In-Situ Calibration and Trajectory Enhancement of UAV LiDAR Systems for Mapping Mechanized Agricultural Fields

Raja Manish ® and Ayman Habib ®, *Member, IEEE*

Abstract—Uncrewed aerial vehicles (UAVs) carrying sensors, such as light detection and ranging (LiDAR) and multiband cameras georeferenced by an onboard global navigation satellite system/inertial navigation system (GNSS/INS), have become a popular means to quickly acquire near-proximal agricultural remote sensing data. These platforms have bridged the gap between high-altitude airborne and ground-based measurements. UAV data acquisitions also allow for surveying remote sites that are logistically difficult to access from ground. With that said, deriving well-georeferenced mapping products from these mobile mapping systems is contingent on accurate determination of platform trajectory along with intersensor positional and rotational relationships, that is, the mounting parameters of various sensors with respect to the GNSS/INS unit. Conventional techniques for estimating LiDAR mounting parameters (also referred to as LiDAR system calibration) require carefully planned trajectory and target configuration. Such techniques are time-consuming, and in certain cases, not feasible to accomplish. In this article, an in-situ system calibration and trajectory enhancement strategy for UAV LiDAR is proposed. The strategy uses planting geometry in mechanized agricultural fields through an automated procedure for feature extraction/matching and using them to enhance the quality of LiDAR-derived point clouds. The proposed approach is qualitatively and quantitatively evaluated using calibration datasets as well as separately acquired validation datasets to demonstrate the performance of the developed procedure. Quantitatively, the accuracy of the resulting UAV point clouds after system calibration and an accompanying trajectory enhancement improved from as much as 43 to 4 cm.

Index Terms—Direct georeferencing, field-based phenotyping, in-situ calibration, light detection and ranging (LiDAR), mobile mapping system (MMS), row/alley extraction, uncrewed aerial vehicle (UAV).

I. INTRODUCTION

OVER the last decade, a lot of research on phenotyping has benefitted from the use of aerial remote sensing data, such as those derived from light detection and ranging (LiDAR), RGB, and multispectral/hyperspectral sensors [1], [2], [3], [4],

[5], [6]. For example, these sensing technologies have been used to analyze change in plant height over time under various circumstances [7], [8], as well as to estimate anatomical characteristics and predict biomass [9], [10], [11], [12]. Inarguably, uncrewed aerial vehicles (UAVs)-based mobile mapping systems (MMSs) have become a valuable phenotyping tool in advancing key research on seed breeding trials. Among the various sensors, RGB and multispectral/hyperspectral cameras are used to acquire images in several electromagnetic spectral bands. On the other hand, LiDAR are ranging sensors, and they have the ability to travel through gaps between leaves and acquire points from under-canopy plant structures and ground. Despite the different functionalities, information derived from any of the above sensors is only as good as the quality of their georeferencing. In general, most UAV MMSs are equipped with a global navigation satellite system/inertial navigation system (GNSS/INS) unit that is used for direct georeferencing of their sensor data. However, direct georeferencing requires precise estimates of translational and rotational offsets between the GNSS/INS unit and various sensors. In the case of a LiDAR unit (which is the focus of this article), by estimating its translational and rotational offsets relative to the GNSS/INS unit—the process is also known as LiDAR system calibration—one can transform any raw LiDAR data to a global coordinate frame. Conventional LiDAR system calibration techniques are often time-consuming and require special skills and artificial targets [13], [14], [15], [16], [17], [18], [19]. This means that circumstances of limited time availability and lack of artificial targets for calibration may lead to a significant delay in the onsite deployment of MMS in agricultural fields. Moreover, even a mission-ready system is prone to unforeseen scenarios of equipment mishandling during its transportation. With the further increase in demand for these MMS, it is therefore imperative that an alternative technique for LiDAR system calibration is explored. In this article, an in-situ LiDAR system calibration and trajectory refinement strategy are developed that can directly use point cloud data acquired over agricultural fields, particularly those that are used for seed breeding trials. As in the case of the conventional-feature-based calibration approach, the proposed method relies on geometric features available in point clouds from field data acquisitions.

The rest of the article is organized as follows. In Section II, the concept of system calibration is introduced with a brief background on intrinsic sensor parameters and mounting parameters
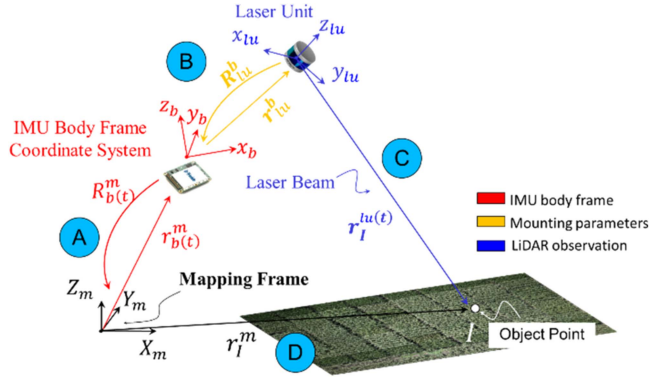
Fig. 1. Illustration of the vectors and quantities involved in the LiDAR point positioning equation for 3-D reconstruction of a LiDAR point cloud.

Fig. 2. Impact of inaccurate mounting parameters on the alignment of point clouds.

relating the georeferencing and LiDAR units; then, a review of related work on LiDAR system calibration is presented in Section III. This is followed by Section IV, which introduces the MMS and datasets used in this article. Thereafter, in Sections V and VI, the proposed methodology is explained in detail with supporting experiments and their results. In Section VI, the resulting point clouds from the experiments are qualitatively and quantitatively assessed, and the performance of the proposed strategy is validated using conventional artificial targets. Finally, Section VII concludes this article.

II. BACKGROUND: LiDAR SYSTEM CALIBRATION

LiDAR system calibration refers to determining the intrinsic sensor parameters as well as the relative mounting parameters of the LiDAR unit. These parameters are needed to define the laser beam orientation with respect to the body frame of GNSS/INS's inertial measurement unit (IMU). The system calibration is based on a mathematical model that relates the position of a point in the LiDAR unit frame to the corresponding point in the mapping frame through a coordinate transformation, as represented by (1). The transformation takes into account the absolute position and orientation of the georeferencing unit and its translational/rotational offsets relative to the LiDAR. A schematic diagram of the LiDAR point positioning equation is shown in Fig. 1. In this diagram, the point positioning equation refers to the summation of three vectors ($\vec{A}$, $\vec{B}$, and $\vec{C}$) defined in the mapping frame to derive the object coordinates of the laser beam footprint ($\vec{D}$) [14]. In (1), $r_I^{lu(t)}$ represents the position of an object point in the LiDAR unit frame at the time of the laser pulse t. The position and orientation of the platform body, i.e., the IMU coordinate frame, with respect to the mapping frame at time t, are denoted by $r_{b(t)}^m$ and $R_{b(t)}^m$, respectively. The mounting parameters that relate the LiDAR unit frame to the platform body are represented by the time-invariant lever arm r_{lu}^b and boresight matrix R_{lu}^b. Last, the coordinates of the LiDAR point I in the mapping frame are denoted by r_I^m

$$r_I^m = r_{b(t)}^m + R_{b(t)}^m r_{lu}^b + R_{b(t)}^m R_{lu}^b r_I^{lu(t)}. \qquad (1)$$

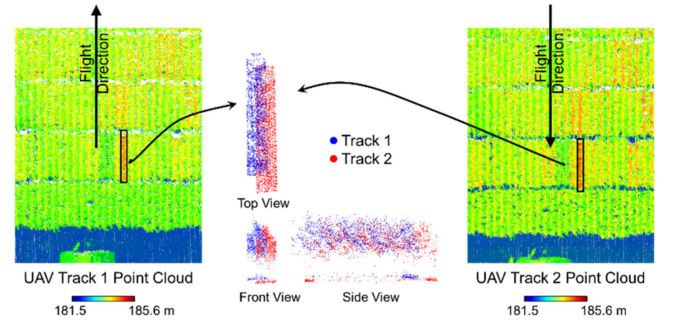It is important to mention that for the LiDAR units considered in this article, their internal characteristic parameters, which define certain properties of the laser beam, such as its firing angle and footprint relative to the LiDAR unit, are provided by the manufacturer. In other words, the laser rangefinders in LiDAR are typically factory calibrated with a high precision. On the other hand, the external characteristic (or mounting) parameters that relate the LiDAR unit to the IMU body frame must be estimated and refined through a system calibration procedure. One should note that a bias might still be present in the intrinsic parameters and may vary over time with sensor usage. Those biases, however, will have much less impact on the LiDAR point cloud compared to resulting discrepancies from incorrect estimates of the mounting parameters. Hence, the internal sensor parameters are not considered in the proposed methodology.

To illustrate the impact of these parameters on point cloud quality, Fig. 2 shows sample agricultural point clouds acquired from two different UAV flight tracks within the same mission and a common region selected for the assessment. As a result of inaccurate mounting parameters, conjugate segments from the highlighted regions exhibit misalignment between them. Moreover, an inaccurate trajectory may also introduce misalignment among corresponding features. Thus, the focus of this article is the refinement of LiDAR mounting and trajectory parameters through an in-situ system calibration and trajectory enhancement approach. Conceptually, these parameters are estimated through an optimization procedure, which minimizes discrepancies among identifiable conjugate features, such as plant rows and ground patches extracted from LiDAR point clouds.

III. RELATED WORK ON IN-SITU SYSTEM CALIBRATION

As discussed in the previous section, accurate knowledge of the mounting parameters is necessary to correctly transform raw scans onto a global coordinate system. Most of the prior work on in-situ LiDAR calibration can be categorized into four groups as follows.

1) In-situ calibration focused only on enhancing the internal characteristic parameters of static terrestrial laser scanners (TLS) or multibeam LiDAR units.
2) In-situ calibration techniques to determine LiDAR mounting parameters for terrestrial mapping platforms.
3) In-situ calibration techniques to determine mounting parameters for airborne or UAV-mounted LiDAR systems.

4) In-situ multimodal sensor calibration techniques involving two or more LiDAR units, or a combination of camera and LiDAR sensors to assist with the calibration.

A. In-Situ Calibration Focused Only on Enhancing the Internal Characteristic Parameters of Static Terrestrial Laser Scanners (TLS) or Multibeam Lidar Units

Early work related to in-situ calibration focused mainly on enhancing the internal characteristic parameters of static TLS or multibeam LiDAR units [20], [21], [22], [23], [24]. Since these systems do not have a georeferencing unit, the reconstructed point clouds are manually georeferenced using control points. Chan and Lichti [25] demonstrated an automatic in-situ calibration of a multibeam Velodyne HDL32e LiDAR in static and kinematic modes by mounting the unit on a tripod and a vehicle, respectively. In their approach, objects observed in each LiDAR scan, such as lamp posts, were extracted and modeled as three-dimensional (3-D) cylindrical features in order to estimate the LiDAR's internal systematic errors. As the calibration was performed entirely in the LiDAR unit frame, measurements from a georeferencing unit were not used. In a similar work, Kim et al. [26] stressed on periodic recalibration of LiDAR units with a primary focus on their internal characteristic parameters. They used planar features to minimize systematic errors associated with multibeam LiDAR. As a drawback, their experiments were limited to scanning indoor environments using a backpack system.

B. In-Situ Calibration Techniques to Determine LiDAR Mounting Parameters for Terrestrial Mapping Platforms

Among some in-situ calibration techniques that targeted LiDAR mounting parameters, Mirzaei et al. [15] used a planar checkerboard target to estimate both the internal characteristic parameters of a 64-beam Velodyne LiDAR as well as the external transformation between the LiDAR unit and a spherical vision system mounted on the same platform. On the downside, they only considered static scenarios, and their method involved manual movement of the platform within a calibration site comprised of planar targets. Gong et al. [27] proposed an approach to determine LiDAR-to-camera transformation by using trihedral building structures observed in different epochs. Chan et al. [28] proposed an in-situ calibration technique that used ground planes and power cables in point clouds for estimating boresight angles between 2-D scanners mounted on a terrestrial platform and the platform's body frame. This approach can be helpful for LiDAR calibration in locations near roadways, where there are few or no building structures. All the above methods target ground-based platforms.

C. In-Situ Calibration Techniques to Determine Mounting Parameters for Airborne or UAV-Mounted LiDAR Systems

Several authors have centered their work on airborne or UAV-mounted LiDAR systems. It is important to mention that different studies estimated either only the boresight parameters or both the lever arm and boresight parameters, depending on their developed procedure. Filin [29] proposed a system calibration method for airborne laser scanners (ALS) using natural terrain and emphasized that well-distributed slopes with different orientations are required for accurate calibration. Skaloud and Lichti [30] presented an in-situ boresight self-calibration of ALS. The calibration was conducted by optimizing LiDAR points from different scans to fit a common plane model. The authors noted that planar features from buildings, particularly tilted ones, were more effective than ground patches. Kumari et al. [31] estimated the mounting parameters for an ALS through an adjustment of systematic errors among conjugate ground surfaces by conducting an iterative closest point (ICP)-based point cloud registration. Lee et al. [32] proposed a similar ALS calibration technique that implemented a correlation-based matching of surface profiles. Guo et al. [33] obtained boresight parameters for their UAV LiDAR through an approach similar to that in Skaloud and Lichti [30]. Oliveira and Dos Santos [34] developed a sequential approach of estimating and refining UAV LiDAR system calibration parameters. Datasets were acquired in a built-up area which facilitated the identification and extraction of gabled building roofs as planar features. Subsequently, these features were utilized in a point-to-plane distance minimization approach for refining the mounting parameters. Li et al. [35] similarly performed a rigorous boresight calibration using UAV LiDAR point clouds from urban areas. The point clouds were segmented and matched within overlapping regions to determine the required rigid body transformation for coarse registration. It was subsequently followed by an ICP-based fine registration. These coarse and fine registration steps sequentially refine the boresight parameters necessary to improve the alignment of point clouds. Like the above studies, Keyetieu and Seube [36] used features from terrain slopes and buildings to conduct boresight adjustment. Rodrigues dos Santos et al. [37] applied a combination of morphological filter and random sample consensus on building structures to identify and extract planar features, such as gabled roofs. Then, a triangular irregular network (TIN) correspondence model was incorporated to estimate boresight misalignment by minimizing the sum of normal distances between points and corresponding TIN patches. Their method was able to reduce the point-to-TIN patch distance from about 1.2 to 0.8 cm. Yu et al. [13] proposed a calibration technique using planar features and artificial spherical targets for point cloud registration. They claimed a registration accuracy range of 0.009–0.07 m across four datasets. Dharmadasa et al. [38] used building features, such as edges and slopes, from overlapping scans and aligned them by heuristically modifying the boresight parameters. Several attempts were required to achieve a satisfactory alignment.

D. In-Situ Multimodal Sensor Calibration Techniques Involving Two or More LiDAR Units, or a Combination of Camera and Lidar Sensors to ASSIST With the Calibration

Some studies have proposed multimodal sensor calibration techniques involving two or more LiDAR sensors, or a combination of camera and LiDAR sensors to assist with the calibration. Cortes et al. [39] performed a combined bundle adjustment

(BA) for their UAV MMS to obtain camera–LiDAR mounting parameters. They emphasized the need to consider georeferencing uncertainty in the calibration. Ravi et al. [14] developed a feature-based calibration approach for multimodal MMS that does not require special calibration targets. One of the limitations of their proposed method is the need to manually extract features from point clouds. Zhou et al. [40] performed the extrinsic calibration of camera and LiDAR with only a few targets using 3-D line-to-plane correspondences. Elbahnasawy et al. [41] proposed an integration of LiDAR and image points in a BA for simultaneous calibration of the two sensors. Zhou et al. [42] developed an automated in-situ calibration approach based on a tightly coupled camera–LiDAR integration workflow for UAV systems. At first, a GNSS/INS-assisted structure from motion (SFM) strategy is implemented on camera imagery to generate image-based point clouds. Thereupon, feature correspondences between the image-based and LiDAR point clouds are identified through an automated procedure. Finally, an integrated-BA is conducted that incorporates image points, raw LiDAR measurements, and GNSS/INS information to estimate system calibration parameters. Through experiments, the authors reported an absolute accuracy of 3–5 cm for image and LiDAR point clouds. More recently, Tian et al. [43] determined lever arm and boresight parameters separately in two steps. The lever arm parameters were estimated with the help of ground control points and SFM modeling using camera images. On the other hand, the boresight parameters were refined by conducting an ICP-based point cloud registration.

Although a lot of work has been done on LiDAR system calibration, none of them simultaneously addresses the following.

1) A true in-situ calibration of UAV LiDAR using a dataset that would eventually reach an end-user instead of obtaining separate calibration data (for example, an approach suitable for mechanized agricultural fields).
2) A method that relies primarily on georeferenced point clouds from the candidate LiDAR unit with little or no aid from a secondary LiDAR or camera (i.e., point clouds from the candidate LiDAR alone are used to provide plenty of features for a reliable and accurate calibration).
3) Refinement of trajectory parameters in addition to LiDAR system calibration.
4) Minimal amount of user effort in feature extraction, i.e., a fully automatic procedure.

Thus, a new strategy is desired that addresses the aforementioned limitations. In this article, we present the development of an in-situ calibration and trajectory enhancement approach that uses the planting geometry of mechanized agricultural fields to establish feature correspondences and perform a feature-based LiDAR system calibration with the possibility of refining the trajectory.

IV. UAV MAPPING SYSTEMS AND DATASETS DESCRIPTION

Two UAV systems are used in this article, namely UAV–LRGB-1 and UAV–LRGB-2, as shown in Fig. 3. Both systems feature the same sensor integration configuration, as pictured in Fig. 3(a). The UAV–LRGB-1 consists of a DJI Matrice 600
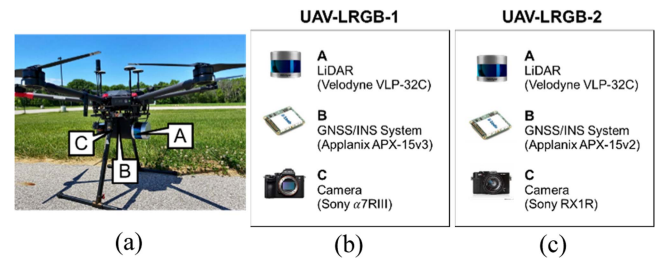

Fig. 3. Details of the UAV systems used in this article. (a) UAV with integrated sensors. (b) Components of UAV–LRGB-1. (c) Components of UAV–LRGB-2.

Pro hexacopter equipped with a Velodyne VLP-32C LiDAR unit, a Sony α7R III RGB camera, and an Applanix APX-15v3 GNSS/INS unit for direct georeferencing. The VLP-32C is a multibeam LiDAR consisting of 32 laser rangefinders mounted radially in a vertical plane with a 40° FOV from +15° to −25° about the horizontal. The entire laser assembly spins about the unit's vertical axis, which results in a 360° horizontal FOV. The LiDAR has a pulse repetition rate of 600 000 points/s in single return mode at a maximum range of 200 m and a range accuracy of ±3 cm (Velodyne VLP-32C Data Sheet, 2023). The GNSS/INS unit has a postprocessing positional accuracy of ±2–5 cm and roll/pitch and heading accuracy of ±0.025° and ±0.08°, respectively (Applanix APX-15 Datasheet, 2023). The expected accuracy of the derived point cloud based on the georeferencing and LiDAR specifications is evaluated using an error propagation calculator developed by Habib et al. [46]. At a flying height of 50 m, the expected accuracy at nadir is in the range of ±5 − 6 cm. For the second system used in this article, i.e., UAV–LRGB-2, the only difference between the two platforms is in the RGB camera; UAV–LRGB-2 is equipped with a Sony RX1R mirrorless camera.

Two datasets, one from each platform, were collected over a mechanized maize field used for seed breeding trials located at Purdue University's agronomy center for research and education, West Lafayette, IN, USA. The surveyed field, together with the UAV flight lines/tracks are shown in Fig. 4(a). Seed breeding trials involve studying variation in crop yield based on factors, such as the genetic background of seed, time of sowing, and soil nutrition content. As such, for each trial, seeds are sown in consistently spaced plant rows and are grouped into plots where these plots have gaps along the plant rows known as alleys. Fig. 4(b) illustrates the characteristics of the mechanized field used in this article on aerial imagery as well as LiDAR point cloud. The plant rows have a nominal spacing of approximately 76 cm, according to the planter's specification. Alleys also have the same width. It is noteworthy that, due to the differing nature of experiments, plant growth varies from plot to plot, as shown by the varying heights of the LiDAR point cloud in Fig. 4(b). This variability forms the basis for the subsequent development in this article.

Along with the field surveys, two additional datasets were acquired using the two platforms to validate the calibration results. For these validation datasets, the UAV systems were flown over conventional calibration targets and other man-made

TABLE I
DATASETS USED IN THIS ARTICLE

Mission type	Date	System	Number of tracks	Sensor-to-object distance	Track-to-track lateral distance	Row spacing	Alley-to-alley distance
System calibration	2022/08/10	UAV-LRGB-1 / UAV-LRGB-2	11	44 m	~9.5 m	0.76 m	5.3 m
Validation	2022/09/16	UAV-LRGB-1 / UAV-LRGB-2	18	20/40/60 m	2/3/4 m	N/A	N/A

(a)

(b)
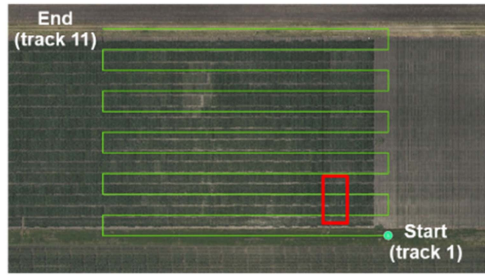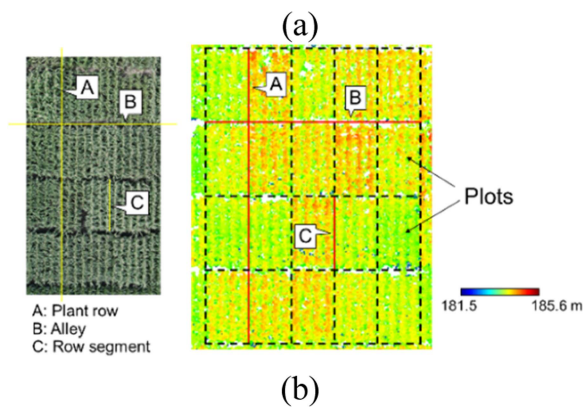
Fig. 4. Location of the surveyed field and UAV mission plan along with an illustration of various planting terminologies common in mechanized fields for seed breeding trials.
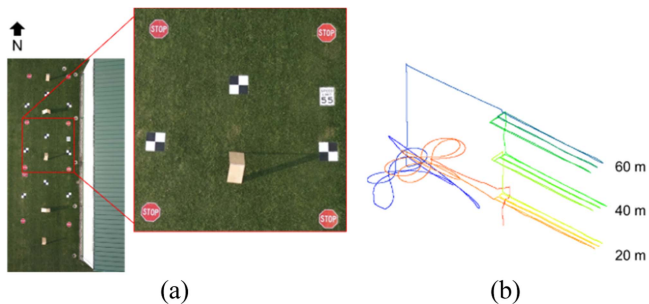

Fig. 5. Target and flight configuration at the study site for the validation dataset: (a) target layout, and (b) UAV flight trajectory colored by time.

infrastructure. Fig. 5(a) shows the types of target features used in the mission: high-reflectivity checkerboards, wooden huts, rooftops, walls, and ground. Moreover, the UAV missions were designed to include multiple parallel flight lines to capture targets from different viewing geometry. Fig. 5(b) visualizes the mission trajectory with flying heights of 20, 40, and 60 m, and lateral separations of 2, 3, and 4 m, respectively. Table I lists the flight details of all four datasets, denoted by their mission type and the corresponding platform names. Both platforms had the same mission plan for their respective missions.

V. METHODOLOGY

This section describes the proposed strategy for LiDAR system calibration and trajectory enhancement. Initially, the platforms are assumed to have coarsely calibrated LiDAR units. Alternatively, approximations of the mounting parameters can also be based on the knowledge of sensor installation. As long as these nominal mounting parameters are reasonably accurate—particularly, if boresight parameters are within a few degrees from the true boresight—the derived point clouds can be used for identifying various planting features, as introduced in Section IV. These features—plant rows, alleys, and ground patches, are then matched across different tracks and used in a system-driven approach for minimizing discrepancies among them while refining the mounting parameters and/or platform trajectory. It is worth noting, however, that a sequential implementation is required for such a technique to avoid any correlation among system calibration and trajectory parameters. Thus, in a two-step approach, the first run refines the calibration, followed by a second run for the trajectory enhancement. Moreover, the system calibration, with or without trajectory enhancement, can be implemented iteratively by using the updated mounting parameters (and trajectory) to reconstruct a new set of point clouds for a second iteration of feature extraction and parameter refinement.

Fig. 6 presents the data processing workflow. It is comprised of 1) generation of point clouds from different tracks using a coarse set of the calibration parameters, 2) aboveground/bare-Earth (AG/BE) point separation, 3) identification of rows and alleys in AG point cloud from each track, 4) matching rows across different tracks through a height-based correlation scheme, 5) feature extraction from individual row segments, and 6) least squares optimization for mounting parameter refinement and trajectory enhancement. The procedure is entirely automated. Moreover, some of the workflow components (feature extraction and matching) have been parallelized to improve the algorithm's performance. A parallel execution allows for running the operation on multiple tracks simultaneously, thereby reducing the
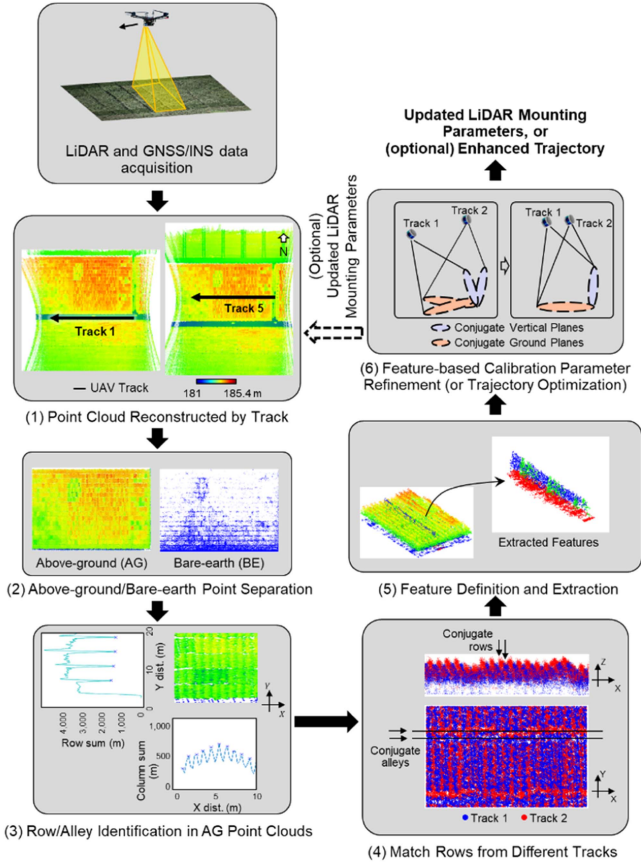
Fig. 6. Workflow of the proposed calibration (and optional trajectory enhancement) procedure.
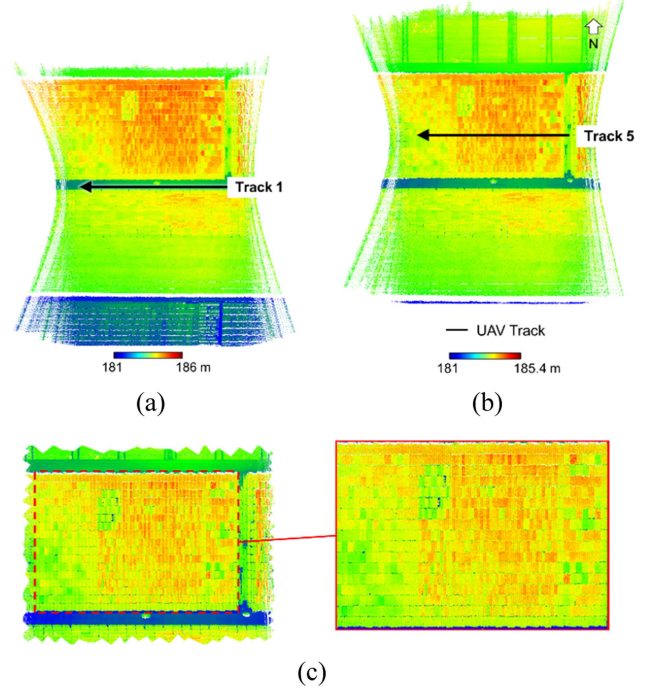

Fig. 7. Point cloud coverage for two UAV flight tracks: (a) track 1, (b) track 5, and (c) region selected for row/alley identification (point clouds are from UAV-LRGB-1).
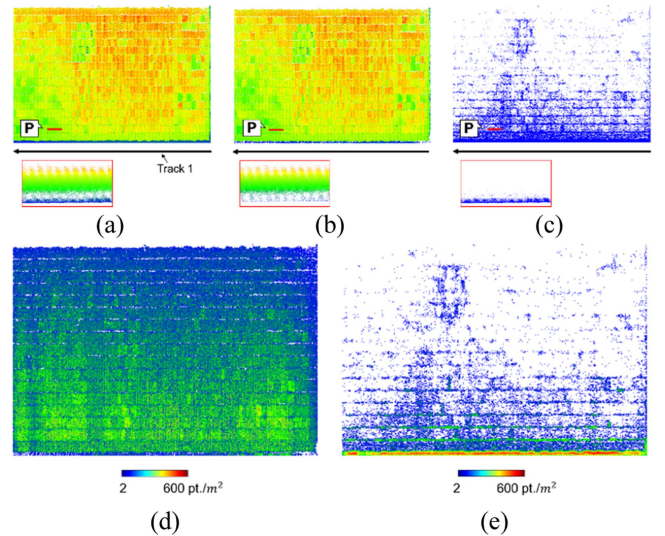

Fig. 8. AG/BE point separation from the selected region of track 1 point cloud with profiles showing side views: (a) entire point cloud, (b) AG points, (c) BE points, (d) point density map of AG points, and (e) point density map of BE points.

processing time. In the subsequent sections, each of the automated processing steps, from feature extraction and matching to mounting parameter refinement or trajectory optimization, will be discussed in detail.

A. Point Cloud Reconstruction From Individual Tracks and AG/BE Point Separation

For the developed methodology, the UAV systems are flown in parallel flight lines or tracks with overlapping ground coverage. Fig. 7(a) and (b) shows the overlap between point clouds from two different flight tracks reconstructed with an off-nadir range of $\pm 110°$. The overlap allows for identifying feature correspondences, which are used in the optimization process. Fig. 7(c) shows the region selected for further analysis in this article.

For each point cloud reconstructed by track, points above the ground, which mostly consist of LiDAR returns from plants, are separated from the ground points. This facilitates the identification of rows and alleys in each track. The AG/BE separation is conducted based on the modified cloth simulation approach proposed by Lin and Habib [47]. The modified approach improves the original cloth simulation by Zhang et al. [48] to generate a more complete digital terrain model in areas with sparse point distribution along the ground. This is often observed in agricultural field datasets when plant canopy located at significant distance from the sensor limits LiDAR returns from the

ground. Fig. 8 shows sample AG/BE point clouds derived from track 1 of the UAV–LRGB-1 platform. For each of the AG and BE point clouds, Fig. 8(d) and (e) visualizes the corresponding point density maps. From the two figures, one can easily notice the varying sparsity of AG/BE points as we move away from the track's projection onto the ground. The increasing sparsity increases the probability of errors in AB/BE point classification, particularly for far regions with few or no points. To avoid the
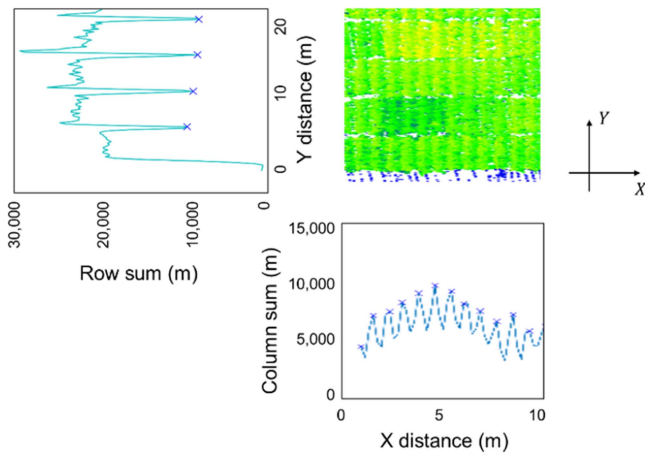
Fig. 9. Identification of plant row/alley locations based on column/row sum of elevation of points (point cloud is colored by height).

inclusion of incorrectly classified AG/BE points in the subsequent processing, only those points that are within a certain lateral distance from individual tracks are included in the point cloud.

B. Row/Alley Identification in AG Points

With the AG/BE points separated, plant rows and alleys are identified in AG points based on the method developed by Lin and Habib [47]. In this method, the point cloud is first rotated to a local coordinate system, say *XY*, in such a way that plant rows and alleys lie along the *Y* and *X* axes, respectively. Note that a precise knowledge of the planting orientation is not required as long as the plant rows are within a few degrees of the *Y*-axis. Then, 2-D cells of a user-specified size are created along the two axes and the sum of elevation of all points within each cell is computed. The hypothesis is that plant locations in the point cloud will have a higher point density. Therefore, the sums of elevation along the *rows* and *columns* of the defined 2-D cells will result in a pattern where local peaks in the *column* sum and local valleys in the *row* sum will indicate plant row and alley locations, respectively [47]. Fig. 9 illustrates the row/alley detection approach, where row locations are characterized by peaks when *column* sums are plotted against distance along the *X*-axis. Similarly, alleys are identified as negative peaks in the *row* sum plot against distance along the *Y*-axis. As previously mentioned, for this approach to work, the quality of point clouds reconstructed using coarse calibration parameters must be adequate to differentiate individual rows as well as identify gaps between row segments. Given the LiDAR's FOV, UAV flying height, and planting pattern, one can evaluate a reasonable boresight misalignment beyond which the row segments might not be distinguishable. It was found that a range of $\pm 2°$ was tolerable for the initial reconstruction.

C. Row Matching Among Tracks

In this step, rows (and alleys) from different flight tracks are matched to identify feature correspondences. A straight-forward method for matching rows and alleys could be based on spatial
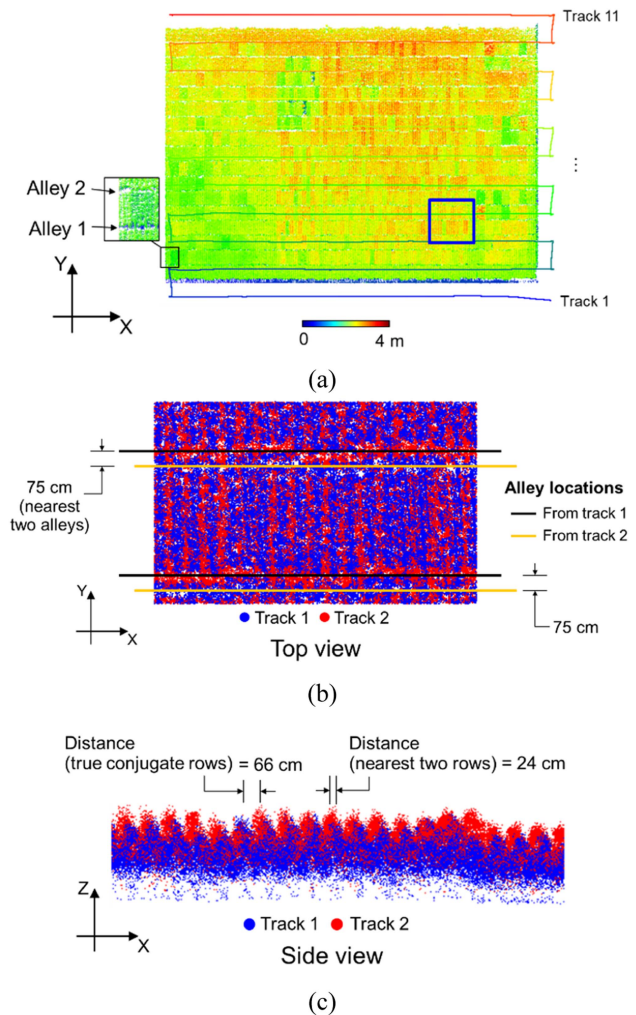

Fig. 10. Misalignment of rows/alleys due to inaccurate mounting parameters illustrated with point clouds from a highlighted region: (a) point cloud with the highlighted region, (b) along-row misalignment between alley locations, and (c) across-row misalignment.

proximity, for example, based on the Euclidian distance (in horizontal plane) between row/alley centers. A row can be matched with the nearest row from another track such that the matched row pair has the minimum Euclidean distance between their centers compared to other possible matches. Similarly, alley centers can be matched with those from other tracks using the same principle. It is worth mentioning however, since point clouds from individual tracks are reconstructed using inaccurate/nominal LiDAR mounting parameters, conjugate rows/alleys may have large discrepancies across/along rows. Fig. 10 visualizes a section of point clouds from two flight tracks with side and top views. For this example, row/alley matches were manually conducted. In Fig. 10(b), one can tell that a matching based on spatial proximity can be reliably performed for alleys given the large ratio of center-to-center distance to the calibration-related misalignment. On the other hand, a proximity-based technique would be difficult to implement for matching rows if across-row discrepancies are larger than half the nominal spacing between the rows, i.e., 38 cm for this field, as shown in Fig. 10(c).
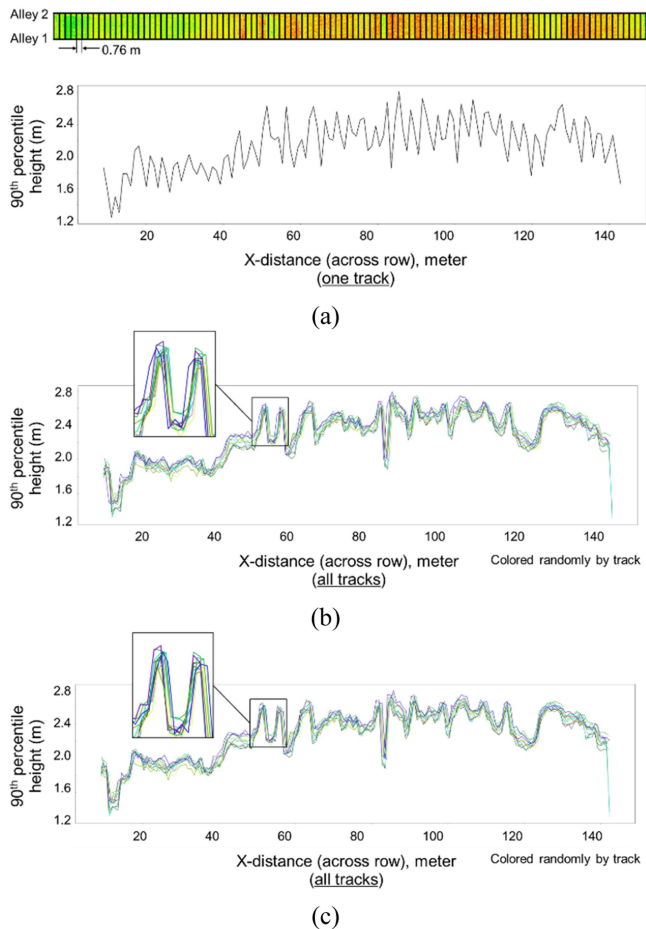
Fig. 11. Height distribution of row segments between two alleys for point clouds from UAV–LRGB-1: (a) point cloud divided into cells and 90th percentile height distribution for one track, (b) height distribution for all 11 tracks before matching, and (c) height distribution of all tracks after matching, i.e., after applying the necessary shifts required to achieve the highest correlation.

Instead of proximity-based row matching, the proposed approach in this article uses a height-based correlation between track pairs to establish an accurate match among row segments. It is based on the hypothesis that the distribution of row segments' average heights over the field will be correlated among all tracks. When two such distributions are analyzed mathematically, the positional shift that results in the highest (positive) correlation will correspond to the best possible match between the two distributions. Such a correlation-based procedure is applicable for any field data that exhibits variation in plant height from one plot to another, as discussed in Section IV. Fig. 11 visualizes the height distribution profiles of row segments between alleys 1 and 2 for all 11 tracks of the uncalibrated UAV–LRGB-1 platform. The procedure for determining height-based correlation can be summarized in the following steps.

1) In the first step, points contained within two neighboring alleys in an overlapping region of two tracks are cropped from the point clouds.
2) Then, these point cloud segments are divided into rectangular cells of equal width similar to the nominal row spacing (0.76 m) across-row (along X-direction), where

the cells are centered at the row location. The cell height corresponds to the length of the row segment.
3) From these cells, a 90th percentile height of points is determined for the entire across-row length, and the same is performed for all tracks, as shown in Fig. 11.
4) Using these 90th percentile height profiles from different tracks, a cross-correlation is computed between a user-defined reference (usually track 1) and all other tracks.

Mathematically, a cross-correlation between two datasets (here, tracks) is represented by (2), where f and g are the input height profiles, N is the total number of cells, n is the displacement or shift between the two profiles, and $\overline{\langle\cdot\rangle}$ denotes the complex conjugate of its content

$$(f \star g)[n] \triangleq \sum_{m=0}^{N-1} \overline{f[m]} g[m+n]. \tag{2}$$

By determining the shift needed to obtain the highest correlation, it is possible to match two different height profiles, and thus match row segments. It is worth mentioning that the matching procedure need only be performed for row segments between a single pair of successive alleys unless such region of the point cloud had been excluded due to point sparsity. In that case, for the affected tracks, row segments from a different pair of successive alleys should be considered. Fig. 11(c) visualizes the outcome of the matching procedure when applied to all 11 tracks of the UAV–LRGB-1 dataset.

D. Geometric Feature Extraction

In this step, various geometric primitives are identified and modeled using points extracted from each row segment. These primitives, which can be classified as planar and linear features, essentially provide necessary control in various directions. All these planar and linear primitives are used in an optimization framework to minimize discrepancies among conjugate features from different tracks while enhancing mounting or trajectory parameters. The selection of these features is motivated by the geometry of the planting pattern in mechanized agricultural fields used for seed breeding trials (these fields often use a precise planter with GNSS-assisted autosteer functionality). The well-defined rows and alleys enable easy identification of individual row segments. For the agricultural field datasets used in this article, Fig. 12 visualizes the three feature types—two planar and one linear, that are extracted from each row segment and used in the developed procedure. Among the three feature types, a near-vertical planar feature is defined using 3-D points along the crop stalks within a row segment. Similarly, a horizontal plane can be defined by the BE points for a given row segment. Last, a linear, near vertical, feature of user-defined width is derived from the start and end of each row segment, providing control in the third direction. The start/end of row segments are determined by observing sudden changes in the row sum plot (these sudden changes represent the end and beginning of the alley separating two neighboring plots). It is important to mention that due to the sparsity of point clouds at a given location, not all features can be identified (and therefore extracted) from each row segment. In Fig. 12, one of the row segments (*row segment 1*) does not
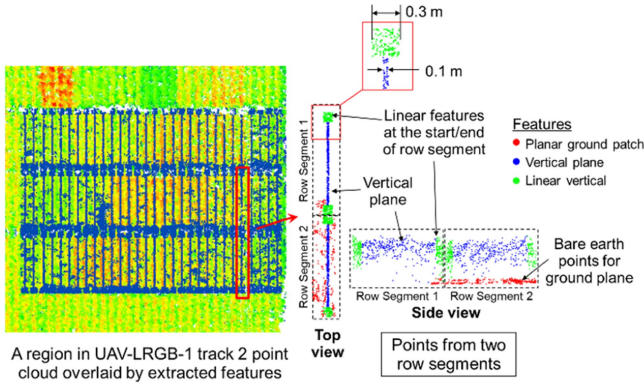
Fig. 12.   Types of features extracted from each track.

Fig. 13.   Discrepancy between 3-D point pairs for (a) linear and (b) planar features.

have enough BE points to correctly define a ground plane. Nonetheless, the datasets used in the article have 11 tracks, providing sufficient feature redundancy. Therefore, the absence of features from a few tracks would not affect the optimization accuracy.

E. LiDAR System Calibration and Trajectory Enhancement

Once the features from all tracks have been extracted and matched, an optimization procedure is implemented that minimizes discrepancies between the matched features while refining the mounting parameters. It is important to note that the UAV's GNSS/INS trajectory is usually considered to be of the best quality possible. Yet, if necessary, trajectory parameters can also be corrected for errors following the same principle as the mounting parameters. When it comes to trajectory, one might argue that trajectory enhancement alone could resolve point cloud misalignments. Such an assumption is risky, however, since an independently conducted trajectory enhancement might mask any discrepancies caused by biases in the mounting parameters. Therefore, a trajectory enhancement should be conducted after the mounting parameters have been refined. Conceptually, in the optimization step, extracted features are utilized in an iterative least squares adjustment (LSA) that minimizes normal distances between feature points and the respective parametric model of the extracted feature until a predefined normal distance threshold is achieved [14], [49]. The optimization is based on the point positioning equation [as introduced earlier by (1)] to refine the LiDAR-to-body-frame mounting parameters, r_{lu}^b and R_{lu}^b, or the trajectory parameters, $r_{b(t)}^m$ and $R_{b(t)}^m$, expressed symbolically by (3) and (4). In (4), $r_I^m(t)_{\text{corrected}}$ are the corrected coordinates of the LiDAR point $r_I^m(t)$ obtained after system calibration (or after trajectory enhancement following system calibration). Thus, the corrected coordinates will depend on the refined mounting parameters (r_{lu}^b(refined), R_{lu}^b(refined)), or the combination of both the refined mounting parameters as well as the estimated corrections to the trajectory position and orientation parameters, $\delta r_{b(t)}^m$ and $\delta R_{b(t)}^m$, respectively. Usually, trajectory corrections are not solved for every laser pulse timestamp, as that would lead to overparameterization in the LSA. Given the moderate platform dynamics in the case of UAVs, the original high-frequency trajectory is downsampled
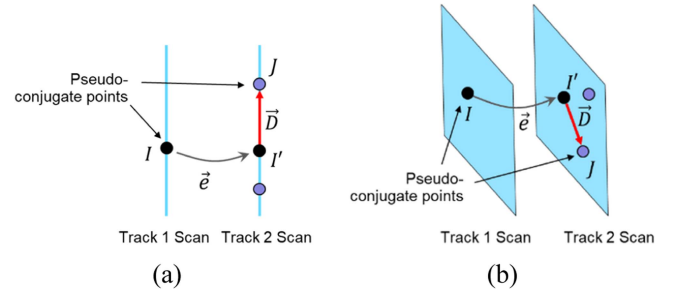
to a user-defined rate, where the downsampled timestamps are referred to as trajectory reference points. Then, the corrections to the trajectory at each laser pulse timestamp are modeled as pth order polynomial functions of estimated corrections to their n neighboring reference points

$$r_I^m(t) = f\left(r_{b(t)}^m,\ R_{b(t)}^m,\ r_{lu}^b,\ R_{lu}^b,\ r_I^{lu(t)}\right) \tag{3}$$

$$r_I^m(t)_{\text{corrected}} = f\left(\begin{array}{c} r_{b(t)}^m, \delta r_{b(t)}^m,\ R_{b(t)}^m, \delta R_{b(t)}^m, \\ r_{lu}^b\ (\text{refined}),\ R_{lu}^b\ (\text{refined}),\ r_I^{lu(t)} \end{array}\right). \tag{4}$$

Fig. 13 illustrates the concept of discrepancy minimization for conjugate linear and planar features. Due to the irregular distribution of point clouds, point-to-point correspondences cannot be used in this procedure. As such, the minimization is conducted between pseudoconjugate 3-D points along corresponding linear/planar features following the mathematical expression given by (5). In the case of linear features, discrepancies between 3-D point pairs (denoted as the random misclosure vector $\vec{e}$) are minimized along the two directions that are normal to the axis of the reference feature. On the other hand, for planar features, discrepancies only along the normal vector of the reference feature are minimized. Vector $\vec{D}$ is the nonrandom component of the discrepancy positioned along the feature. In (6), $\vec{e}$ is normally distributed with zero mean, and its variance–covariance matrix is obtained from the product of a priori variance factor σ_0^2 and weight matrix P. The weight matrix is eventually modified to P' for each feature type to ensure that the unknown vectors $\vec{D}$ along the features are eliminated [49]. The LSA subsequently results in updated system calibration parameters, or trajectory parameters if enhanced following the calibration

$$r_I^m - r_J^m = \vec{D} + \vec{e} \tag{5}$$

$$\vec{e} \sim \left(0, \sigma_0^2 P^{-1}\right),\ P'\ \vec{D} = 0. \tag{6}$$

VI. EXPERIMENTAL RESULTS AND DISCUSSION

The proposed strategy for LiDAR system calibration and trajectory enhancement was implemented for each of the two UAV systems using the previously defined features extracted and matched across different tracks. For feature extraction, the width of cloud for the fitted vertical and ground planar features is set to 0.1 m, as illustrated in Fig. 12. Likewise, the vertical

TABLE II
NUMBER OF UNIQUE LINEAR AND PLANAR FEATURES (AND POINTS)
EXTRACTED FROM THE TWO FIELD DATASETS

	UAV–LRGB-1	UAV–LRGB-2
Number of unique planar and linear features	523 and 440	528 and 470
Number of LiDAR points in the features	1 006 761	1 030 539

linear features have cross-sectional dimensions of $0.3\,\text{m} \times 0.3\,\text{m}$. These values were empirically determined for UAV datasets based on the sparsity of points within the features. It is worth mentioning that the features need not be extracted from all rows as long as the overall area covered is large. In the current experiment, only every 10th row is used for the features, for a total of 17 rows out of about 170 in the field. Table II reports the specifics of the extracted features for the two datasets. For both experiments, the initial mounting parameters are user-defined based on direct measurement of the lever arm together with a reasonable approximation of the boresight angles. Results from an earlier calibration could also be used for the boresight angles. One should note that having a constant flying height for different tracks will lead to a high correlation among the lever arm and boresight angles [50]. Hence, the lever arm parameters were set as constants during the estimation of boresight angles.

A. Results

The results of the LSA were evaluated both qualitatively and quantitatively. Table III summarizes the initial and estimated mounting parameters together with their standard deviations (STDs) after the LSA. One can notice that the STD values are very small. At this point, if there is a need to enhance the trajectory, a second LSA is conducted. In this sequential approach, the refined mounting parameters estimated from the first LSA are fixed, followed by evaluating the corrections for the trajectory reference points. Figs. 14 and 15 show feature points, respectively, for the two datasets before and after calibration, as well as after the sequential calibration and trajectory enhancement. In both figures, it can be seen from the different views that the alignment of features has improved after each LSA process. The refined mounting parameters result in an improvement in the point cloud quality in all three directions. However, small misalignments may still exist, as seen in Fig. 14(c) and (d) and Fig. 15(c) and (d) for X and Y directions, which are then reduced with the second LSA, i.e., after trajectory enhancement. From the two figures, one can see a significant improvement in feature alignment after the sequential LSA processes.

To demonstrate the changes in trajectory parameters, Fig. 16 shows individual tracks from the UAV–LRGB-1 trajectory, colored by applied distance and angular corrections. It is worth mentioning that the characteristics of applied corrections are similar for the UAV–LRGB-2 trajectory, and therefore not visualized. Table IV shows the root mean of squared (rms) corrections for all six trajectory parameters. The values in Table IV indicate
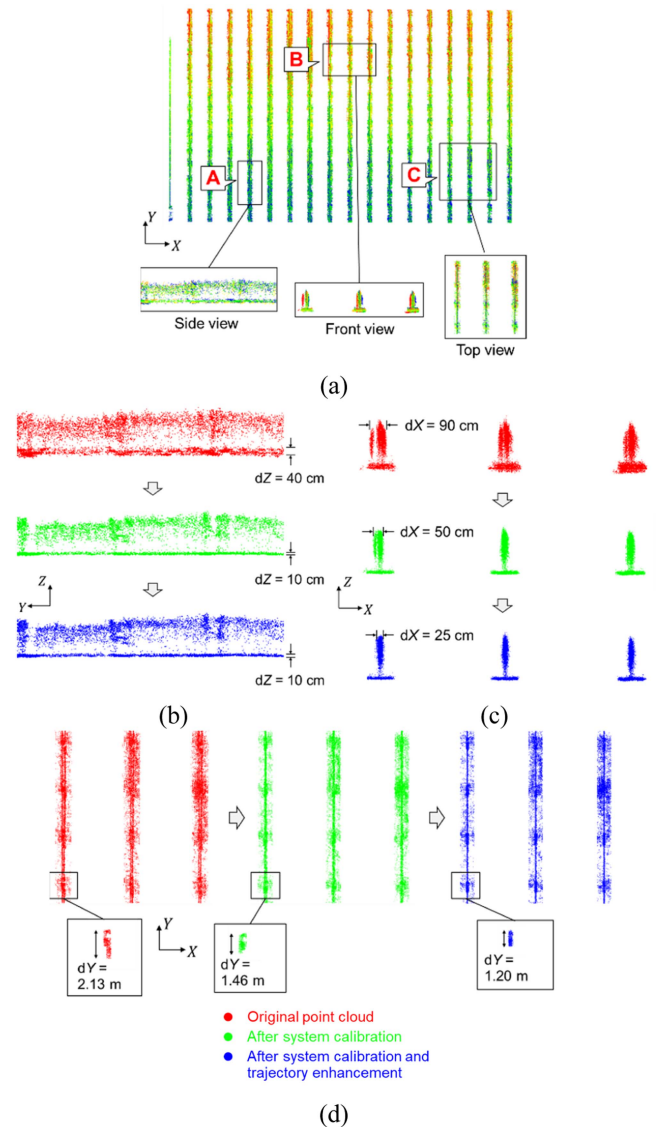

Fig. 14. Alignment of sample UAV–LRGB-1 features before and after system calibration, as well as after system calibration and trajectory enhancement: (a) top view of the extracted features before calibration (colored by time) and selected regions in different views, (b) region A, (c) region B, and (d) region C.

that the distance corrections observed in the lateral (Y) direction were relatively higher than those in forward (X) and vertical (Z) directions. As for the angular corrections, the ω component (corresponding to the platform roll) is relatively higher than ϕ (pitch) and κ (heading). For the quantitative evaluation of the proposed calibration and trajectory enhancement strategy, Table V reports the rms normal distances of points to their corresponding feature parametric model. The proposed approach enhances feature alignment in both datasets. Most notably, for UAV–LRGB-2, the linear feature fitting RMSE reduces from over a meter in the original point cloud to about 20 cm after refinement. This value is in agreement with the cross-sectional dimensions of the vertical features defined earlier in this section. It is worth noting that the values listed in Table V and those annotated in Figs. 14 and 15 are different. The latter are samples representing double the normal distances used to derive the

TABLE III
LiDAR MOUNTING PARAMETERS BEFORE AND AFTER REFINEMENT

	Mounting parameters	ΔX (m)	ΔY (m)	ΔZ (m)	$\Delta\omega$ (°)	$\Delta\phi$ (°)	$\Delta\kappa$ (°)
UAV–LRGB-1	Initial	−0.130	0.030	0.000	0.000	0.000	0.000
	Refined	−0.130	0.030	0.000	0.471 ±0.0004	−0.204 ±0.0002	−0.164 ±0.0005
UAV–LRGB-2	Initial	0.010	0.040	0.100	0.000	0.000	0.000
	Refined	0.010	0.040	0.100	1.092 ±0.0004	−0.079 ±0.0003	−0.134 ±0.0006

TABLE IV
ROOT MEAN OF SQUARED CORRECTIONS APPLIED TO
TRAJECTORY PARAMETERS

	X (cm)	Y (cm)	Z (cm)	ω (°)	ϕ (°)	κ (°)
UAV–LRGB-1	0.27	0.86	0.62	0.117	0.098	0.084
UAV–LRGB-2	0.25	1.20	0.91	0.129	0.100	0.078

TABLE V
QUANTITATIVE EVALUATION OF THE POINT CLOUD ALIGNMENT BEFORE
SYSTEM CALIBRATION, AFTER SYSTEM CALIBRATION, AND AFTER
TRAJECTORY ENHANCEMENT FOLLOWING SYSTEM CALIBRATION

Dataset	Feature type	Number of feature points	RMSE Before calibration (m)	RMSE After calibration (m)	RMSE After calibration and trajectory enhancement (m)
UAV–LRGB-1	Linear	202 559	0.333	0.258	0.187
	Planar	804 202	0.431	0.072	0.041
UAV–LRGB-2	Linear	222 817	1.158	0.404	0.204
	Planar	807 722	0.434	0.188	0.041

TABLE VI
COMPARISON OF THE ESTIMATED BORESIGHT PARAMETERS FOR THE
TWO SYSTEMS

UAV–LRGB-1			
Calibration method	$\Delta\omega$ (°)	$\Delta\phi$ (°)	$\Delta\kappa$ (°)
Proposed	0.471	-0.204	-0.164
Conventional	0.458	-0.127	-0.218
UAV–LRGB-2			
Calibration method	$\Delta\omega$ (°)	$\Delta\phi$ (°)	$\Delta\kappa$ (°)
Proposed	1.092	-0.079	-0.134
Conventional	1.062	-0.024	-0.166

B. Validation

In the previous section, the performance of the proposed system calibration (as well as the sequential system calibration and trajectory enhancement) approach was evaluated using features extracted from row segments. In this section, the accuracy of refined mounting parameters is validated using additional UAV datasets acquired over conventional calibration targets, as introduced in Section IV. The validation procedure assumes that the LiDAR units remained rigidly mounted over time between the two acquisition dates. Following the GNSS/INS postprocessing, point clouds from different flight tracks are reconstructed using the original (initialized) and refined mounting parameters. Finally, for the qualitative and quantitative assessment of the point clouds, several calibration targets comprising retroreflective sign boards and huts are manually extracted from these point clouds.

Table VI presents the estimated boresight parameters for the two datasets from both the proposed as well as conventional approaches. The maximum difference in the parameter values is under $0.08°$. Fig. 18 shows the alignment quality of reflective targets for the UAV–LRGB-1 and UAV–LRGB-2 datasets reconstructed using mounting parameters from the uncalibrated system and the proposed calibration technique. While the targets in the original "uncalibrated" point clouds appear noisy and indistinguishable, those extracted from the point clouds based on the proposed calibration technique are significantly less noisy and are easy to identify. Fig. 19 shows the alignment quality of huts positioned along the north–south and east–west directions in the UAV point clouds. One can see that the proposed approach
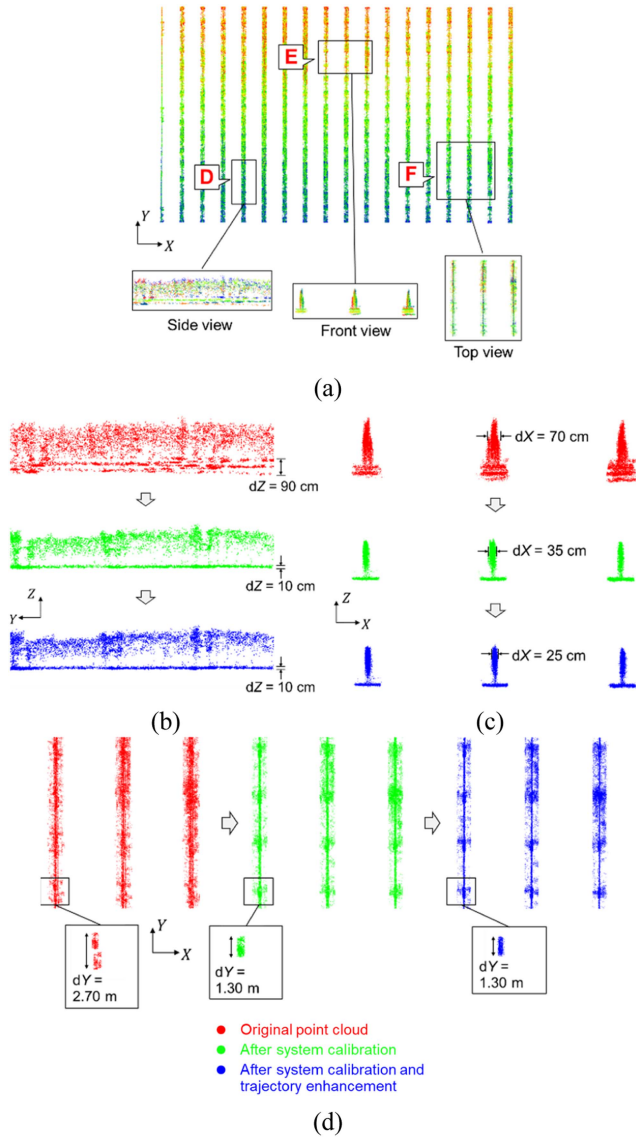
statistics in Table V (i.e., the normal distances for the samples are expected to be multiples of the rms measures in Table V with a factor of 2 to 3, considering the 99.7% range of discrepancies that follow a normal distribution).

For a better insight into the impact of calibration and system trajectory enhancement on reconstructed point clouds, two profiles: one across-row (P1) and one along-row (P2), were manually extracted from reconstructed point clouds, as in Fig. 17. In Fig. 17(b) and (d), individual rows and alleys can be distinctly identified in UAV–LRGB-1 point clouds reconstructed using the refined calibration or calibration and trajectory parameters. An identical observation can be made in Fig. 17(c) and (e) for UAV–LRGB-2. In general, ground and row segments have better alignment among tracks following system calibration and trajectory enhancement, indicating an overall high quality of point cloud alignment.

Fig. 15. Alignment of sample UAV–LRGB-2 features before and after system calibration, as well as after system calibration and trajectory enhancement: (a) top view of the extracted features before calibration (colored by time) and selected regions in different views, (b) region D, (c) region E, and (d) region F.
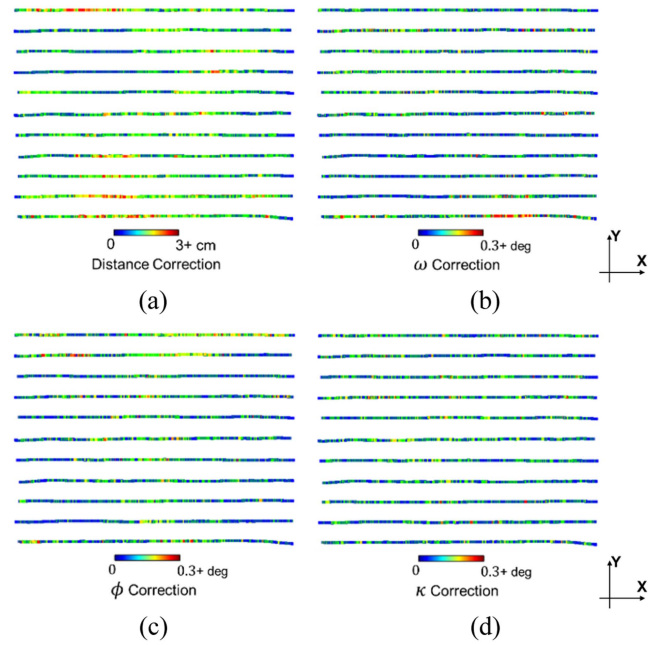

Fig. 16. UAV–LRGB-1 tracks colored by the magnitude of applied distance and angular corrections to the GNSS/INS trajectory: (a) distance corrections, (b) ω corrections, (c) ϕ corrections, and (d) κ corrections.

can be attributed to the lever arm components that were derived through manual measurements and fixed in the LSA.

C. Discussion

The results from the proposed system calibration and trajectory enhancement technique suggest that the strategy developed in this article has the potential to determine accurate boresight parameters and, if needed, refine the platform position and orientation. Through the proposed method, discrepancies among point clouds from different calibration tracks were reduced by 65, 140, and 80 cm in the across-row, along-row, and vertical directions, respectively. The validation results also demonstrated the effectiveness of the technique toward achieving high relative accuracy of adjusted point clouds. The absolute accuracy is verified by the alignment of point clouds from two UAV systems whose data have been independently processed. Among the planar and linear features used in this article, the control provided by the linear features (along plant rows) was limited due to the sparseness of the point cloud along the individual row segments. As such, the procedure may benefit from further investigation into the more precise derivation of along-row features. Compared to traditional calibration strategies, which require the deployment of calibration targets, the proposed work is more practical. It eliminates the user effort required during data acquisition and processing. The feature extraction and matching processes are automated. Moreover, the entire calibration and trajectory enhancement procedure utilizes data typically acquired data over seed breeding trials. Thus, the method can be considered a valuable alternative in scenarios with limited calibration opportunities. In terms of calibration accuracy, removing the fixed lever arm constraint, as previously
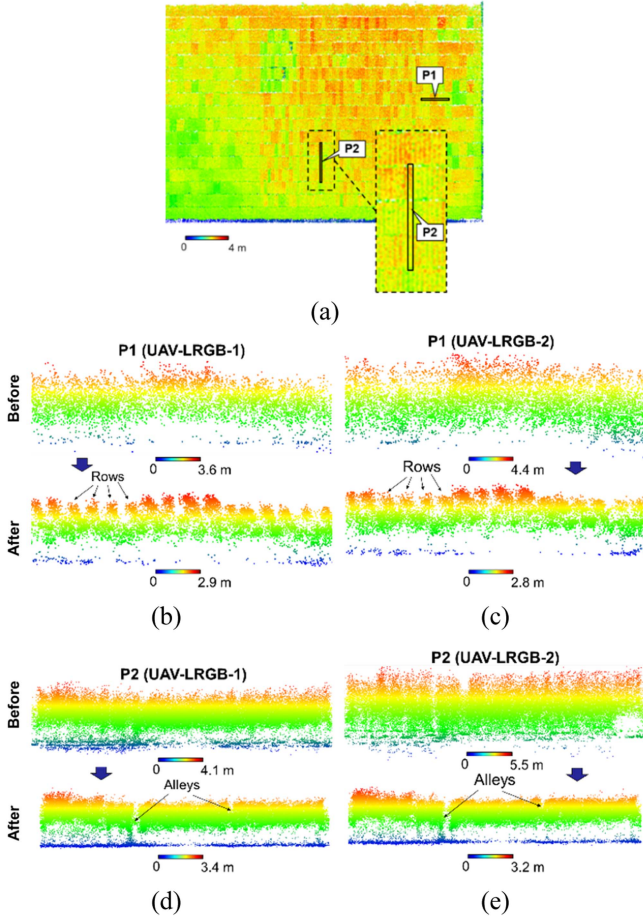
results in a significant improvement of the alignment in all three directions.

While the above assessment investigates the relative accuracy of individual UAV datasets following the proposed system calibration, analyzing the alignment of point clouds from the two platforms together may provide further indications for their absolute accuracy. This comes from the fact that the datasets UAV–LRGB-1 and UAV–LRGB-2 are independently acquired and processed in an absolute reference frame. Fig. 20 shows four different hut features extracted from the two UAV datasets after system calibration through the proposed and conventional approaches. From the figure, one can clearly see that the features are well-aligned in the planimetric direction. A small misalignment exists in the north–south and vertical directions, which

(a)

Fig. 17. Point cloud alignment (for all tracks) before and after system calibration and trajectory enhancement: (a) profile locations on UAV–LRGB-1 point cloud, (b) **P1** (across-row) in UAV–LRGB-1, (c) **P1** (across-row) in UAV–LRGB-2, (d) **P2** (along-row) in UAV–LRGB-1, and (e) **P2** (along-row) in UAV–LRGB-2 (point clouds are colored by height).
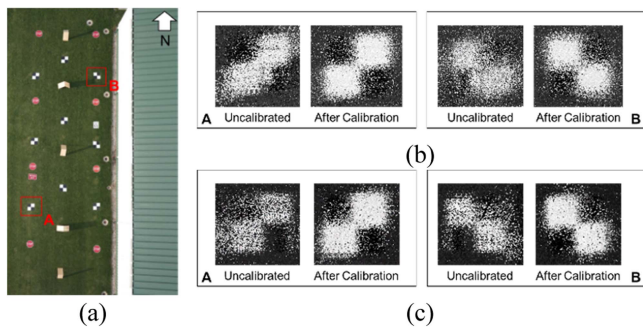

Fig. 18. Qualitative evaluation of 2-D alignment of reflective targets before and after system calibration: (a) targets selected for comparison, (b) UAV–LRGB-1 point cloud, and (c) UAV–LRGB-2 point cloud (point clouds are from all 18 tracks and are colored by intensity).
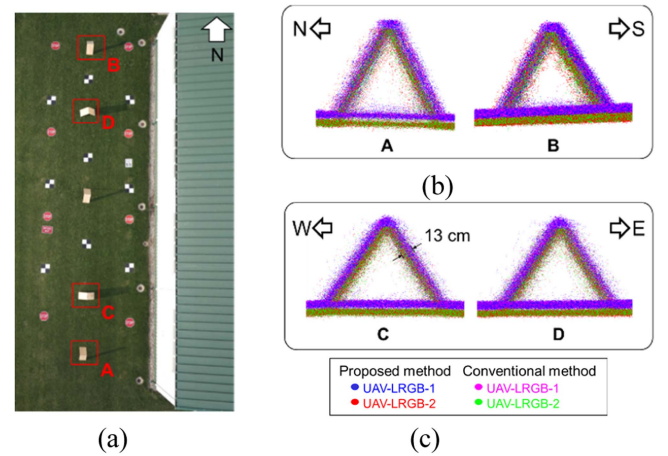

Fig. 19. Qualitative evaluation of 3-D alignment of huts along north–south and east–west directions before and after system calibration: (a) targets selected for comparison, (b) UAV–LRGB-1 point cloud, and (c) UAV–LRGB-2 point cloud (point clouds are from all 18 tracks and are colored by intensity).

Fig. 20. 3-D alignment of hut targets for the UAV–LRGB-1 and UAV–LRGB-2 datasets: (a) targets selected for comparison, (b) alignment along north–south direction, and (c) alignment along east–west direction.

TABLE VII
AVERAGE PROCESSING TIME FOR FEATURE EXTRACTION AND MATCHING

Data size	Feature extraction/matching time (for 16-core CPU and 64 GB RAM)
One track (175 rows)	∼110 s
All tracks (1,925 rows)	∼1,200 s

discussed, may result in more accurate estimates of the mounting parameters, provided the UAV is flown at multiple flying heights. Table VII enumerates the average feature extraction/matching time needed to process each dataset used in this article. It should be noted that the algorithm allows for adjusting the number of features to be extracted (therefore adjusting the processing time)

depending on the redundancy requirement. The performance can be further improved by employing a more powerful workstation with additional cores, larger RAM capacity, and faster read/write capable hard drive.

VII. Conclusion

UAV-based data acquisitions for high-throughput phenotyping are often conducted in mechanized agricultural fields. The UAV LiDAR system calibration and trajectory enhancement strategy developed in this article leverages onsite data acquired from such fields in its implementation. The performance of the proposed strategy was evaluated on two UAV platforms. The results after system calibration followed by trajectory enhancement show a reduction in feature-fitting error for linear features from over 1 m to 20 cm, and for planar features from 43 to 4 cm. The method developed in this article offers several advantages as follows.

1) It allows for using actual agricultural datasets as opposed to flying separate calibration missions, i.e., there is no need for specialized target or building structures for feature extraction.
2) Along with system calibration, the developed approach can also enhance UAV trajectory in a sequential process.
3) The entire process is automated, requiring no supervision.
4) It can be valuable in scenarios where logistic restrictions prevent proceeding with the conventional calibration.

The calibration precision achieved by the developed method is sufficient for most UAV LiDAR applications. Further improvement in techniques for feature extraction and matching, especially for fields with irregular planting patterns, can be studied as a part of future development. Such fields may have rows without alleys, crops in the early season offering little or no height variations, or crops with a nonplanar stalk distribution. On that note, generalizing the technique for different application areas, such as forestry, can also be explored. Such developments might as well benefit from the simultaneous integration of multitemporal datasets from UAVs and ground-based mapping platforms.

Acknowledgment

References

[1] P. Radoglou-Grammatikis, P. Sarigiannidis, T. Lagkas, and I. Moscholios, "A compilation of UAV applications for precision agriculture," *Comput. Netw.*, vol. 172, May 2020, Art. no. 107148, doi: 10.1016/j.comnet.2020.107148.

[2] R. Raj, S. Kar, R. Nandan, and A. Jagarlapudi, "Precision agriculture and unmanned aerial vehicles (UAVs)," in *Unmanned Aerial Vehicle: Applications in Agriculture and Environment*. Cham, Switzerland: Springer, 2020, pp. 7–23, doi: 10.1007/978-3-030-27157-2_2.

[3] D. C. Tsouros, S. Bibi, and P. G. Sarigiannidis, "A review on UAV-based applications for precision agriculture," *Information (Switzerland)*, vol. 10, no. 11, 2019, Art. no. 349, doi: 10.3390/info10110349.

[4] T. Adão et al., "Hyperspectral imaging: A review on UAV-based sensors, data processing and applications for agriculture and forestry," *Remote Sens. (Basel)*, vol. 9, no. 11, Nov. 2017, Art. no. 1110, doi: 10.3390/rs9111110.

[5] L. Feng, S. Chen, C. Zhang, Y. Zhang, and Y. He, "A comprehensive review on recent applications of unmanned aerial vehicle remote sensing with various sensors for high-throughput plant phenotyping," *Comput. Electron. Agriculture*, vol. 182, Mar. 2021, Art. no. 106033, doi: 10.1016/j.compag.2021.106033.

[6] C. Xie and C. Yang, "A review on plant high-throughput phenotyping traits using UAV-based sensors," *Comput. Electron. Agriculture*, vol. 178, Nov. 2020, Art. no. 105731, doi: 10.1016/j.compag.2020.105731.

[7] J. Harkel, H. Bartholomeus, and L. Kooistra, "Biomass and crop height estimation of different crops using UAV-based lidar," *Remote Sens.*, vol. 12, no. 1, Dec. 2019, Art. no. 17, doi: 10.3390/RS12010017.

[8] L. Zhou, X. Gu, S. Cheng, G. Yang, M. Shu, and Q. Sun, "Analysis of plant height changes of lodged maize using UAV-LiDAR data," *Agriculture*, vol. 10, no. 5, May 2020, Art. no. 146, doi: 10.3390/AGRICULTURE10050146.

[9] B. Nazeri, "Evaluation of multi-platform LiDAR-based leaf area index estimates over row crops," Ph.D. Dissertation, Purdue Univ. Graduate Sch., Mar. 2021, doi: 10.25394/PGS.14167358.v1.

[10] J. C. Revenga et al., "Above-ground biomass prediction for croplands at a sub-meter resolution using UAV-LiDAR and machine learning methods," *Remote Sens.*, vol. 14, no. 16, Aug. 2022, Art. no. 3912, doi: 10.3390/RS14163912.

[11] Y. Shendryk, J. Sofonia, R. Garrard, Y. Rist, D. Skocaj, and P. Thorburn, "Fine-scale prediction of biomass and leaf nitrogen content in sugarcane using UAV LiDAR and multispectral imaging," *Int. J. Appl. Earth Observ. Geoinf.*, vol. 92, Oct. 2020, Art. no. 102177, doi: 10.1016/j.jag.2020.102177.

[12] S. R. Levick, T. Whiteside, D. A. Loewensteiner, M. Rudge, and R. Bartolo, "Leveraging TLS as a calibration and validation tool for MLS and ULS mapping of Savanna structure and biomass at landscape-scales," *Remote Sens.*, vol. 13, no. 2, Jan. 2021, Art. no. 257, doi: 10.3390/RS13020257.

[13] J. Yu, X. Lu, M. Tian, T. O. Chan, and C. Chen, "Automatic extrinsic self-calibration of mobile LiDAR systems based on planar and spherical features," *Meas. Sci. Technol.*, vol. 32, no. 6, Apr. 2021, Art. no. 065107, doi: 10.1088/1361-6501/ABECEC.

[14] R. Ravi, Y. J. Lin, M. Elbahnasawy, T. Shamseldin, and A. Habib, "Simultaneous system calibration of a multi-LiDAR multicamera mobile mapping platform," *IEEE J. Sel. Topics Appl. Earth Observ. Remote Sens.*, vol. 11, no. 5, pp. 1694–1714, May 2018, doi: 10.1109/JSTARS.2018.2812796.

[15] F. M. Mirzaei, D. G. Kottas, and S. I. Roumeliotis, "3D LIDAR–camera intrinsic and extrinsic calibration: Identifiability and analytical least-squares-based initialization," *Int. J. Robot. Res.*, vol. 31, no. 4, pp. 452–467, Apr. 2012, doi: 10.1177/0278364911435689.

[16] C. X. Guo and S. I. Roumeliotis, "An analytical least-squares solution to the line scan LiDAR-camera extrinsic calibration problem," in *Proc. IEEE Int. Conf. Robot. Automat.*, 2013, pp. 2943–2948, doi: 10.1109/ICRA.2013.6630985.

[17] Q. Zhang and R. Pless, "Extrinsic calibration of a camera and laser range finder (improves camera calibration)," in *Proc. IROS*, 2004, pp. 2301–2306, doi: 10.1109/IROS.2004.1389752.

[18] A.-I. García-Moreno, J.-J. Gonzalez-Barbosa, F.-J. Ornelas-Rodriguez, J. B. Hurtado-Ramos, and M.-N. Primo-Fuentes, "LiDAR and panoramic camera extrinsic calibration approach using a pattern plane," in *Proc. Mex. Conf. Pattern Recognit.*, 2013, pp. 104–113, doi: 10.1007/978-3-642-38989-4_11.

[19] J. E. Ha, "Extrinsic calibration of a camera and laser range finder using a new calibration structure of a plane with a triangular hole," *Int. J. Control Autom. Syst.*, vol. 10, no. 6, pp. 1240–1244, 2012, doi: 10.1007/s12555-012-0619-7.

[20] T. Rabbani, S. Dijkman, F. van den Heuvel, and G. Vosselman, "An integrated approach for modelling and global registration of point clouds," *ISPRS J. Photogrammetry Remote Sens.*, vol. 61, no. 6, pp. 355–370, Feb. 2007, doi: 10.1016/J.ISPRSJPRS.2006.09.006.

[21] K. Bae and D. Lichti, "On-site self-calibration using planar features for terrestrial laser scanners," *Int. Arch. Photogrammetry Remote Sens. Spatial Inf.*, 2007, Accessed: Feb. 6, 2023. [Online]. Available: https://citeseerx.ist.psu.edu/document?repid=rep1&type=pdf&doi=e4f2da5bd64ed7a6e1c0705f33d3593ab1e8e928

[22] C. Glennie and D. D. Lichti, "Static calibration and analysis of the Velodyne HDL-64E S2 for high accuracy mobile scanning," *Remote Sens.*, vol. 2, no. 6, pp. 1610–1624, Jun. 2010, doi: 10.3390/RS2061610.

[23] J. C. K. Chow, D. D. Lichti, C. Glennie, and P. Hartzell, "Improvements to and comparison of static terrestrial LiDAR self-calibration methods," *Sensors*, vol. 13, no. 6, pp. 7224–7249, May 2013, doi: 10.3390/S130607224.

[24] C. Y. Chen and H. J. Chien, "On-site sensor recalibration of a spinning multi-beam LiDAR system using automatically-detected planar targets," *Sensors*, vol. 12, no. 10, pp. 13736–13752, Oct. 2012, doi: 10.3390/S121013736.

[25] T. O. Chan and D. D. Lichti, "Automatic in situ calibration of a spinning beam LiDAR system in static and kinematic modes," *Remote Sens.*, vol. 7, no. 8, pp. 10480–10500, Aug. 2015, doi: 10.3390/RS70810480.

[26] H. S. Kim, Y. Kim, C. Kim, and K. H. Choi, "Kinematic In situ self-calibration of a backpack-based multi-beam LiDAR system," *Appl. Sci.*, vol. 11, no. 3, Jan. 2021, Art. no. 945, doi: 10.3390/APP11030945.

[27] X. Gong, Y. Lin, and J. Liu, "3D LIDAR-camera extrinsic calibration using an arbitrary trihedron," *Sensors*, vol. 13, no. 2, pp. 1902–1918, Feb. 2013, doi: 10.3390/S130201902.

[28] T. O. Chan, D. D. Lichti, and C. L. Glennie, "Multi-feature based boresight self-calibration of a terrestrial mobile mapping system," *IS-PRS J. Photogrammetry Remote Sens.*, vol. 82, pp. 112–124, Aug. 2013, doi: 10.1016/j.isprsjprs.2013.04.005.

[29] S. Filin, "Recovery of systematic biases in laser altimetry data using natural surfaces," *Photogrammetry Eng. Remote Sens.*, vol. 69, no. 11, pp. 1235–1242, 2003, doi: 10.14358/PERS.69.11.1235.

[30] J. Skaloud and D. Lichti, "Rigorous approach to bore-sight self-calibration in airborne laser scanning," *ISPRS J. Photogrammetry Remote Sens.*, vol. 61, no. 1, pp. 47–59, Oct. 2006, doi: 10.1016/J.ISPRSJPRS.2006.07.003.

[31] P. Kumari, W. E. Carter, and R. L. Shrestha, "Adjustment of systematic errors in ALS data through surface matching," *Adv. Space Res.*, vol. 47, no. 10, pp. 1851–1864, May 2011, doi: 10.1016/j.asr.2010.12.015.

[32] D. G. Lee, E. J. Yoo, J. H. Yom, and D. C. Lee, "Strip adjustment of airborne laser scanner data using area-based surface matching," *J. Korean Soc. Surveying, Geodesy, Photogrammetry Cartogr.*, vol. 32, no. 6, pp. 625–635, 2014, doi: 10.7848/KSGPC.2014.32.6.625.

[33] Q. Guo et al., "An integrated UAV-borne LiDAR system for 3D habitat mapping in three forest ecosystems across China," *Int. J. Remote Sens.*, vol. 38, no. 8–10, pp. 2954–2972, May 2017, doi: 10.1080/01431161.2017.1285083.

[34] E. M. de Oliveira Junior and D. R. Dos Santos, "Rigorous calibration of UAV-based LiDAR systems with refinement of the boresight angles using a point-to-plane approach," *Sensors*, vol. 19, no. 23, Nov. 2019, Art. no. 5224, doi: 10.3390/S19235224.

[35] Z. Li, J. Tan, and H. Liu, "Rigorous boresight self-calibration of mobile and UAV LiDAR scanning systems by strip adjustment," *Remote Sens.*, vol. 11, no. 4, Feb. 2019, Art. no. 442, doi: 10.3390/RS11040442.

[36] R. Keyetieu and N. Seube, "Automatic data selection and boresight adjustment of LiDAR systems," *Remote Sens.*, vol. 11, no. 9, May 2019, Art. no. 1087, doi: 10.3390/RS11091087.

[37] D. Rodrigues dos Santos, L. Ercolin Filho, P. Sérgio de Oliveira Jr, and H. Cândido de Oliveira, "Attitude mounting misalignment estimation method for the calibration of UAV LiDAR system by using a TIN-based corresponding model," *J. Appl. Sci. Technol. Trends*, vol. 1, no. 4, pp. 162–168, Dec. 2020, doi: 10.38094/jastt14115.

[38] V. Dharmadasa, C. Kinnard, and M. Baraër, "An accuracy assessment of snow depth measurements in agro-forested environments by UAV Lidar," *Remote Sens. (Basel)*, vol. 14, no. 7, Apr. 2022, Art. no. 1649, doi: 10.3390/RS14071649.

[39] C. Cortes, M. Shahbazi, and P. Ménard, "UAV-LiCAM system development: Calibration and geo-referencing," *Int. Arch. Photogrammetry, Remote Sens. Spatial Inf. Sci.*, vol. XLII–1, no. 1, pp. 107–114, Sep. 2018, doi: 10.5194/ISPRS-ARCHIVES-XLII-1-107-2018.

[40] L. Zhou, Z. Li, and M. Kaess, "Automatic extrinsic calibration of a camera and a 3D LiDAR using line and plane correspondences," in *Proc. IEEE Int. Conf. Intell. Robots Syst.*, Dec. 2018, pp. 5562–5569, doi: 10.1109/IROS.2018.8593660.

[41] M. Elbahnasawy et al., "Multi-sensor integration onboard a UAV-based mobile mapping system for agricultural management," in *Proc. Int. Geosci. Remote Sens. Symp.*, 2018, pp. 3412–3415, doi: 10.1109/IGARSS.2018.8517370.

[42] T. Zhou, S. M. Hasheminasab, and A. Habib, "Tightly-coupled camera/LiDAR integration for point cloud generation from GNSS/INS-assisted UAV mapping systems," *ISPRS J. Photogrammetry Remote Sens.*, vol. 180, pp. 336–356, 2021, doi: 10.1016/j.isprsjprs.2021.08.020.

[43] Y. Tian, Y. Zhao, S. Lei, C. Ji, L. Duan, and V. Sedlák, "Automatic calibration method for airborne LiDAR systems based on approximate corresponding points model," *J. Sens.*, vol. 2022, 2022, Art. no. 4853419, doi: 10.1155/2022/4853419.

[44] "Velodyne LiDAR UltraPuck (VLP-32C) data sheet," Mar. 2023. Accessed: Mar. 7, 2023. [Online]. Available: https://www.velodynelidar.com/products/ultra-puck/

[45] "Applanix APX-15 datasheet," Mar. 2023. Accessed: Mar. 7, 2023. [Online]. Available: https://www.applanix.com/products/dg-uavs.htm

[46] A. Habib, J. Lay, and C. Wong, "Specifications for the quality assurance and quality control of LiDAR systems," Base mapping and Geomatic services of British Columbia, 2006. Accessed: Mar. 7, 2023. [Online]. Available: https://engineering.purdue.edu/CE/Academics/Groups/Geomatics/DPRG/files/LIDARErrorPropagation.zip

[47] Y. C. Lin and A. Habib, "Quality control and crop characterization framework for multi-temporal UAV LiDAR data over mechanized agricultural fields," *Remote Sens. Environ.*, vol. 256, Apr. 2021, Art. no. 112299, doi: 10.1016/J.RSE.2021.112299.

[48] W. Zhang et al., "An easy-to-use airborne LiDAR data filtering method based on cloth simulation," *Remote Sens. (Basel)*, vol. 8, no. 6, Jun. 2016, Art. no. 501, doi: 10.3390/rs8060501.

[49] E. Renaudin, A. Habib, and A. P. Kersting, "Featured-based registration of terrestrial laser scans with minimum overlap using photogrammetric data," *ETRI J.*, vol. 33, no. 4, pp. 517–527, Aug. 2011, doi: 10.4218/etrij.11.1610.0006.

[50] T. Shamseldin, R. Ravi, M. Elbahnasawy, Y.-J. Lin, and A. Habib, "Bias impact analysis and calibration of UAV-based mobile LiDAR system," in *Proc. Int. Geosci. Remote Sens. Symp.*, 2018, pp. 8769–8772, doi: 10.1109/IGARSS.2018.8518163.

Raja Manish received the B.Eng. degree in mechanical engineering from the Pune University, Pune, India, in 2011, and the M.S. degree in aeronautics and astronautics from the Purdue University, West Lafayette, IN, USA, in 2016. He is currently working toward the Ph.D. degree in geomatics with the Lyles School of Civil Engineering, Purdue University, West Lafayette, IN, USA.

His research interests include GNSS-aided inertial navigation, airborne and terrestrial mapping systems, LiDAR point cloud processing, remote sensing sensor integration and calibration, and multisensor data fusion for localization and mapping.

Ayman Habib (Member, IEEE) received the M.Sc. and Ph.D. degrees in photogrammetry from The Ohio State University, Columbus, OH, USA, in 1993 and 1994, respectively.

He is currently the Thomas Page Professor with the Lyles School of Civil Engineering, Purdue University, West Lafayette, IN, USA. His research interests include the fields of terrestrial and aerial mobile mapping systems using GNSS/INS-assisted photogrammetric and LiDAR sensing modalities, UAV-based 3-D mapping, and integration of multimodal, multiplatform, and multitemporal remote sensing data for applications in transportation, infrastructure monitoring, environmental protection, precision agriculture, digital forestry, resource management, and archeology.